

Dark and bright modes, and their coherent control in dipolar metasurface bilayersSaumya Choudhary ^{1,*}, Robert W. Boyd ^{1,2} and J. E. Sipe³¹*Institute of Optics, University of Rochester, Rochester, New York 14627, USA*²*Department of Physics, University of Ottawa, Ottawa, Ontario, Canada K1N 6N5*³*Department of Physics, University of Toronto, Toronto, Ontario, Canada M5S 1A7*

(Received 14 September 2022; accepted 14 February 2023; published 27 February 2023)

Several plasmonic nanoparticles supporting dipolar resonances can couple to form normal modes. Here, we develop an analytical model to explain the formation of nonradiative “dark” and radiative “bright” modes through radiative coupling in bilayers consisting of dipolar nanoantenna arrays that are separated by a subwavelength distance. We also include near-field contributions in our model and show that the absorption and reflectance spectra obtained from our model agree reasonably well with the respective finite-difference time-domain simulation results for both perfectly aligned and misaligned bilayers. The ability to vary the reflection and absorption spectra of these bilayers by changing the material and geometrical parameters has potential applications in the design of efficient spectral filters. We also show that we can selectively excite these modes by adjusting the phase between two counterpropagating normally incident fields, which has applications in all-optical modulators and switches based on purely linear interferometric effects.

DOI: [10.1103/PhysRevA.107.023521](https://doi.org/10.1103/PhysRevA.107.023521)**I. INTRODUCTION**

Noble-metal nanoparticles support localized surface plasmons, which are oscillations of free electrons in the nanoparticle coupled to the electromagnetic field and can lead to strong resonant scattering and absorption of light [1,2]. A collection of these nanoparticles can be used to tailor the scattering and absorption of light at the nanoscale, which has been the subject of extensive research during the past few decades for applications related to cloaking [3,4], wave-front engineering [5–7], harmonic generation [8], and all-optical switching [9,10] and to the properties of materials with artificially engineered parameters such as permittivity and permeability [11–17]. Mode hybridization in a plasmonic dimer, where two identical nanoparticles are placed at a subwavelength separation, has been studied extensively [18–23]. These dimers can support “dark” modes that have a significant local-field enhancement in their interstices. They are “dark” in the sense that, if the variation of the incident field over the dimer is neglected, they cannot be excited because of their vanishing dipole moment [18,21,22].

Dark modes in dimers can, however, be excited by linearly polarized light incident along the dimer axis because of higher-order multipole moments of the structure. The large field enhancement [24] and narrow absorption linewidths, which result because of the weak radiation from these higher-order multipole moments, make these “bilayer” dimer structures a promising platform for nonlinear optical applications [10], including plasmonic nanolasers [25,26]. The antiparallel polarization distribution of these dark modes forms a quasicurrent loop with an effective magnetic dipole,

which can be a useful building block for an effective negative-index material [27,28]. Usually, arrays of these nanostructures are fabricated in order to observe a measurable extinction response. In an array with lattice constants smaller than the dipolar resonance wavelength, the far-field coupling between the nanostructures can modify the radiative damping rate such that it scales proportionally with the number density of nanostructures [29]. Previous studies of cooperative modes in metasurface bilayers were restricted to spherical or disk-shaped nanoparticles made of noble metals with resonances at visible or near-infrared frequencies [30–34]. These nanoparticles have a low scattering efficiency due to their small dipolar polarizability [35–38] and are also affected by the presence of multipolar modes and large absorption losses in most plasmonic materials due to interband transitions at ultraviolet frequencies.

Here, we theoretically investigate bilayers of dipolar nanoantenna arrays separated by a fraction of their dipolar resonance wavelength at near-infrared frequencies. We show that radiative coupling in this bilayer leads to the formation of bright (symmetric) and dark (antisymmetric) modes [39] and discuss how the short-range nonradiative coupling shifts these resonances. We also compare the reflectance and absorption spectra calculated from our analytical model with those obtained from finite-difference time-domain (FDTD) simulations for both perfectly aligned and slightly misaligned bilayers. We show that the dark modes can make a significant contribution to the optical response; although they are weakly driven, their weak radiation rate leads to significant excitation. Finally, we discuss the selective excitation of these dark and bright modes by varying the relative phase between two equal-intensity counterpropagating fields, which is also referred to as the coherent control of absorption [40,41].

*schoudha@ur.rochester.edu

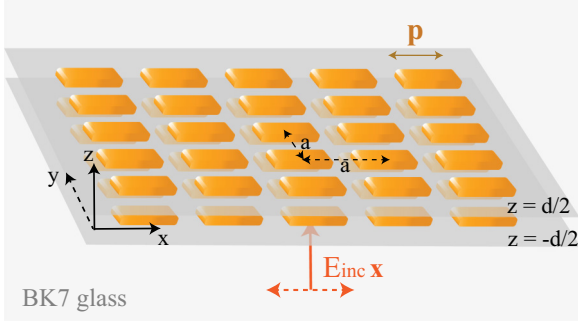


FIG. 1. Diagram of the bilayer structure of two nanoantenna arrays spaced by a separation d and excited by a normally incident plane wave \mathbf{E}_{inc} .

II. ANALYTICAL MODEL

Our structure comprises two square arrays of dipolar nanoantennas that have an in-plane lattice constant of a and are separated by a subwavelength distance d . Figure 1 shows a diagram of the bilayer along with the assumed coordinate system. The first array is assumed to be in the ($z = -d/2$) plane, and the second array is assumed to be in the ($z = d/2$) plane. The bilayer is excited by a plane wave $\mathbf{E}_{\text{inc}} = E_{\text{inc}} e^{i(\tilde{\omega}nz - \omega t)} \hat{\mathbf{x}}$. In our analytic modeling we assume the dipoles are polarized along the x axis. Here, ω is the angular frequency of the field, n is the refractive index of the background medium (assumed to be BK7 glass), and $\tilde{\omega} = \omega/c$.

A. Single nanoantenna array

We follow the method detailed earlier [29] to model the response of a single nanoantenna array. The nanoantennas in the array are modeled as point dipoles with a dipole moment \mathbf{p} that is related to the electrostatic polarizability $\overset{\leftrightarrow}{\alpha}_0$ by the following equation:

$$\mathbf{p} = \epsilon_0 n^2 \overset{\leftrightarrow}{\alpha}_0 \mathbf{E}_{\text{tot}}, \quad (1)$$

where ϵ_0 is the vacuum permittivity, n is the refractive index of the surrounding medium, and \mathbf{E}_{tot} is the electric field at the point dipole, given by

$$\mathbf{E}_{\text{tot}} = \mathbf{E}_{\text{inc}} + \frac{1}{4\pi\epsilon_0} \frac{2}{3} in\tilde{\omega}^3 \mathbf{p} + (\overset{\leftrightarrow}{\beta}_0 + \overset{\leftrightarrow}{\beta}) \cdot \frac{1}{\epsilon_0 n^2} \mathbf{p}. \quad (2)$$

Here, $\mathbf{E}_{\text{inc}} = E_{\text{inc}} \hat{\mathbf{x}}$ is the field incident on the dipole, the second term on the right-hand side of (2) is the radiation reaction of the dipole itself, the purely real dyadic $\overset{\leftrightarrow}{\beta}_0$ is the dynamic depolarization term that accounts for the field retardation over the volume of the nanoantenna, and the dyadic $\overset{\leftrightarrow}{\beta}$ is the dynamic interaction constant of the array that includes the retarded field contributions at the dipole from all the other dipoles in the array [29].

In the chosen coordinate system, $\overset{\leftrightarrow}{\alpha}_0$ is a 3×3 diagonal matrix whose elements $\alpha_{0,ii}$ for $i = \{x, y, z\}$ depend on the material permittivities of the nanoantenna and the surrounding medium, as well as its shape. The resonance frequency ω_0 in the electrostatic limit is given by the condition $\text{Re}[\alpha_{0,ii}^{-1}(\omega_0)] = 0$. We now define an effective polarizability

$\overset{\leftrightarrow}{\alpha}_{\text{shift}}$ that includes the electrostatic response of each nanoantenna along with the resonance shifts due to the retardation contributions $\overset{\leftrightarrow}{\beta}_0$ and $\text{Re}[\overset{\leftrightarrow}{\beta}]$,

$$\overset{\leftrightarrow}{\alpha}_{\text{shift}}^{-1} = \overset{\leftrightarrow}{\alpha}_0^{-1} - \epsilon_0 n^2 (\overset{\leftrightarrow}{\beta}_0 + \text{Re}[\overset{\leftrightarrow}{\beta}]). \quad (3)$$

The term $\text{Im}[\overset{\leftrightarrow}{\alpha}_{\text{shift}}^{-1}]$ is the same as $\text{Im}[\overset{\leftrightarrow}{\alpha}_0^{-1}]$, which accounts for absorption losses in the nanoantenna. The term $\text{Im}[\overset{\leftrightarrow}{\beta}]$ includes the radiation reaction contributions from all the other nanoantennas in the array and, for a linearly polarized excitation along the length of the nanoantenna assumed here (aligned with the x axis), is given by [42]

$$\text{Im}[\beta_{xx}] = -\frac{1}{6\pi} (n\tilde{\omega})^3 + \frac{n\tilde{\omega}}{2a^2}. \quad (4)$$

From Eqs. (1)–(4), we can write, after some simplification,

$$\alpha_{\text{shift},xx}^{-1} p_x = \epsilon_0 n^2 \left(E_{\text{inc}} + \frac{i\tilde{\omega}}{2\epsilon_0 n a^2} p_x \right). \quad (5)$$

We drop the suffixes x from now on, and from (5) we write

$$\alpha_{\text{eff}}^{-1} = \alpha_{\text{shift}}^{-1} - \frac{i\tilde{\omega}n}{2a^2}, \quad (6)$$

where α_{eff} is the polarizability of the nanoantenna defined in terms of the incident field, so that $p = \epsilon_0 n^2 \alpha_{\text{eff}} E_{\text{inc}}$. Figures 2(a) and 2(b) show the spectra of the real and imaginary parts, respectively, of α_0 (blue solid lines), α_{shift} (red dashed lines), and α_{eff} (black dot-dashed lines) of a representative gold nanoantenna in a square lattice with a lattice constant a of 250 nm. The nanoantenna parameters are taken to be the same as those in Choudhary *et al.* [29], and we keep a fixed at 250 nm in all the results presented here. We use the permittivity data from Johnson and Christy for gold [43] and the refractive index data from the Schott optical glass data sheets [44] for the surrounding BK7 glass. The scattering, absorption and extinction cross-section spectra of the nanoantenna are shown in Fig. 7 in Appendix A. As shown in Fig. 2, the effect of the retardation components is to shift the nanoantenna resonance, while the radiation reaction term contributes to its broadening.

We now define the polarization P of the nanoantenna array as the dipole moment per unit area, which is essentially the product of the dipole moment p of a nanoantenna in the array and the number density of these nanoantennas ($= 1/a^2$ for a square array with lattice constant a). So we write

$$P = \frac{\epsilon_0 n^2 \alpha_{\text{eff}}}{a^2} E_{\text{inc}}. \quad (7)$$

The x component of the electric field from this lattice of electric dipoles at a position $(l_1 a + \Delta_x, l_2 a + \Delta_y, z)$, with (l_1, l_2) being the lattice indices in the xy plane and $\Delta_{x,y}$ being the displacements from the lattice points $(l_1 a, l_2 a)$, is given by

$$E_x(\mathbf{R}_l + \mathbf{\Delta}, z) = \frac{i\tilde{\omega}}{2\epsilon_0 n} P e^{i\tilde{\omega}n|z|} + \frac{\pi}{\epsilon_0 a n^2} T_{xx}(\mathbf{\Delta}, z) P, \quad (8)$$

where $\mathbf{R}_l = l_1 a \hat{\mathbf{x}} + l_2 a \hat{\mathbf{y}}$ and $\mathbf{\Delta} = \Delta_x \hat{\mathbf{x}} + \Delta_y \hat{\mathbf{y}}$. The first term on the right is the long-range radiative field, whereas the second term is the short-range near field that decays rapidly

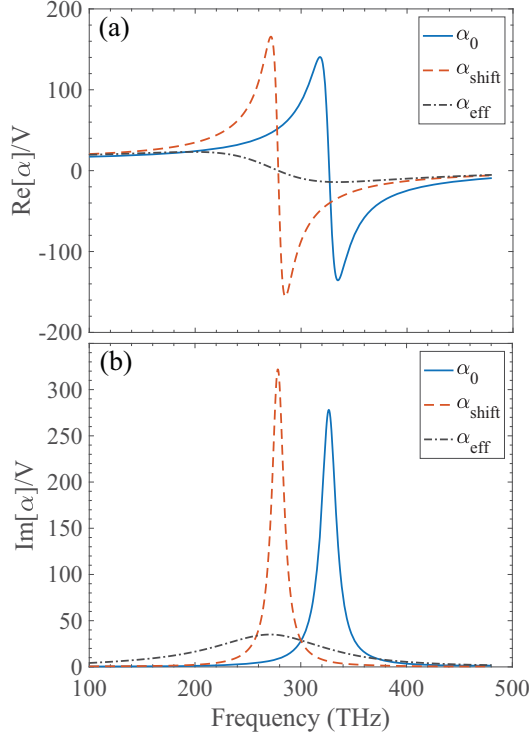


FIG. 2. Spectra of the (a) real and (b) imaginary parts of polarizabilities normalized to the volume of a cuboidal gold nanoantenna (185 nm long, 105 nm wide, and 20 nm thick and embedded in BK7 glass) in the electrostatic limit (blue solid lines), including only the retardation of the nanoantenna and the array (red dashed lines), and including both retardation and the radiation reaction of the nanoantenna and the array (black dot-dashed lines). The nanoantenna polarizability model is taken to be the same as in [29], and the array lattice constant is assumed to be 250 nm.

with z . See Appendix B for the full derivation of (8) and the expression for $T_{xx}(\Delta, z)$.

B. The bilayer structure

We now consider the bilayer structure, wherein the two lattice planes are assumed to be laterally misaligned such that the lattice points in the second (first) plane are displaced by Δ ($-\Delta$) with respect to lattice points in the first (second) plane, with the lattice points then in the first plane. The field at each dipole plane now includes not only the incident field \mathbf{E}_{inc} but also the radiated field and the near field from the other plane. Hence, we can write the polarization of both dipole arrays as

$$P_{2,1} = \frac{\epsilon_0 n^2 \alpha_{\text{eff}}}{a^2} [E_{\text{inc}} e^{\pm i\tilde{\omega}nd/2} + E_x(\pm\Delta, \pm d/2)], \quad (9)$$

where we consider the unit cell to be centered at the origin for simplicity. Multiplying both sides of Eq. (9) by α_{eff}^{-1} and substituting (6), we get, after some simplification,

$$\begin{aligned} \alpha_{\text{shift}}^{-1} P_{2,1} &= \frac{\epsilon_0 n^2}{a^2} E_{\text{inc}} e^{\pm i\tilde{\omega}nd/2} + \frac{i\tilde{\omega}}{2a^2} (P_{2,1} + P_{1,2} e^{i\tilde{\omega}nd}) \\ &\quad \pm \frac{\pi}{a^3} T_{xx}(\Delta, d) P_{1,2}, \end{aligned} \quad (10)$$

where we have used $T_{xx}(\Delta, d) = T_{xx}(-\Delta, -d)$. We then define $P_A = (P_1 + P_2)/2$ and $P_M = (P_2 - P_1)/2$ using (10), the first being the average of the plane polarizations and the second being the difference between them. After some algebraic manipulation, we have

$$P_A = \frac{\epsilon_0 n^2 \alpha_A}{a^2} E_{\text{inc}} \cos(\tilde{\omega}nd/2), \quad (11)$$

$$P_M = i \frac{\epsilon_0 n^2 \alpha_M}{a^2} E_{\text{inc}} \sin(\tilde{\omega}nd/2), \quad (12)$$

where

$$\alpha_A^{-1} = \alpha_{\text{shift}}^{-1} + S(\Delta, d) - \frac{i\tilde{\omega}n}{a^2} \cos^2\left(\frac{\tilde{\omega}nd}{2}\right), \quad (13)$$

$$\alpha_M^{-1} = \alpha_{\text{shift}}^{-1} - S(\Delta, d) - \frac{i\tilde{\omega}n}{a^2} \sin^2\left(\frac{\tilde{\omega}nd}{2}\right), \quad (14)$$

and

$$S(\Delta, d) = \frac{\tilde{\omega}n}{2a^2} \sin(\tilde{\omega}nd) - \frac{\pi}{a^3} T_{xx}(\Delta, d). \quad (15)$$

The resonance frequencies ω_A (ω_M) of the A (M) mode are given by the condition $\text{Re}[\alpha_{A,M}^{-1}] = \text{Re}[\alpha_{\text{shift}}^{-1}] \pm S(\Delta, d) = 0$. Hence, the purely real term $S(\Delta, d)$ leads to equal and opposite shifts in resonances for the A and M modes with respect to the resonance of a single layer. The terms $\text{Im}[\alpha_{A,M}^{-1}]$ include the absorption losses $\text{Im}[\alpha_{\text{shift}}^{-1}]$ and the radiative damping terms given by the last terms on the right in Eqs. (13) and (14). For very small separations d , such that $\tilde{\omega}nd \ll 1$, the symmetric A mode has almost twice the radiative damping as a single layer. In contrast, the radiative damping of the antisymmetric M mode is very small. For such small separations the A mode is a nominally bright mode with a wider linewidth than the single array, while the M mode is a nominally dark mode with a significantly narrower linewidth that, in practice, is limited by absorption losses within the nanoantenna. Hence, at the resonance of the M mode ($\text{Re}[\alpha_M^{-1}] = 0$), the polarizability α_M can be made to be significantly larger than α_{eff} with a careful choice of design parameters a and d . For this condition, the amplitude P_M of the nominally dark mode can be much larger than the amplitude P_A of the nominally bright mode, which essentially implies that the dipole moments of the nanoantennas in the different layers are mostly out of phase. We note that the retardation of the incident field between the two arrays is large enough to allow the excitation of the M mode at normal incidence for even perfectly aligned arrays [45].

Using $P_1 = P_A - P_M$ and $P_2 = P_A + P_M$, we calculate the expressions for the transmittance (T), reflectance (R), and absorbance (A) of the bilayer. The forward-propagating field from the bilayer at a distance $z \gg d/2$ is given by

$$E_{\text{forward}}(z) = e^{i\tilde{\omega}nz} \left[E_{\text{inc}} + \frac{i\tilde{\omega}}{2\epsilon_0 n} (P_1 e^{i\tilde{\omega}nd/2} + P_2 e^{-i\tilde{\omega}nd/2}) \right], \quad (16)$$

where the first term on the right is simply the retarded incident field and the remaining terms are the long-range radiative fields from both nanoantenna arrays. Rewriting P_1 and P_2 in terms of P_A and P_M and using Eqs. (11) and (12), we get, after

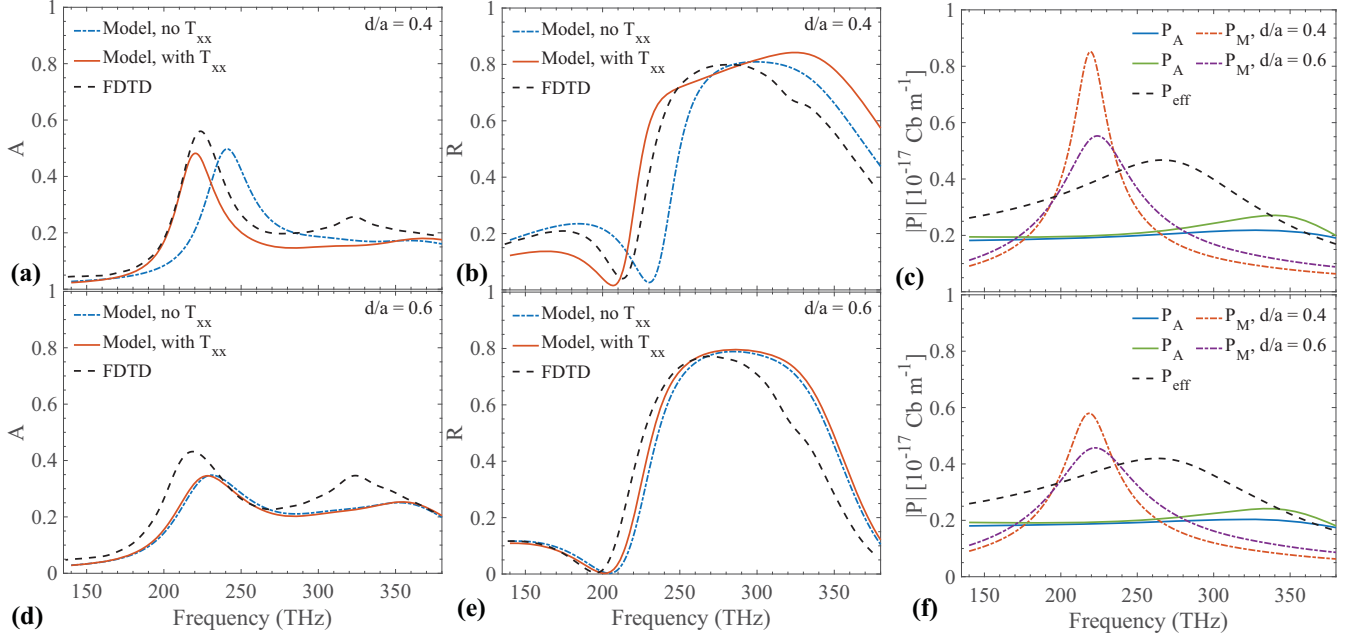


FIG. 3. Absorption spectra of a bilayer structure with no misalignments between the layers and (a) $d/a = 0.4$ and (d) $d/a = 0.6$ obtained from Eqs. (17) and (19) without (blue dot-dashed lines) and with (red solid lines) the near-field terms $T_{xx}(\mathbf{0}, d)$. The black dashed lines are the respective absorption spectra obtained from FDTD simulations. The reflection spectra for the $d/a = 0.4$ and $d/a = 0.6$ structures are shown in (b) and (e), respectively. The polarization spectra of P_A (solid lines) and P_M (dot-dashed lines) for the two aforementioned bilayers without and with absorption losses in the nanoantennas are shown in (c) and (f), respectively, along with P_{eff} for a single nanoantenna plane (black dashed lines) without and with the absorption losses.

some simplification,

$$t \equiv \frac{E_{\text{forward}}(z)}{E_{\text{inc}} e^{i\tilde{\omega}nz}} = 1 + \frac{i\tilde{\omega}n}{a^2} \left(\alpha_A \cos^2 \frac{\tilde{\omega}nd}{2} + \alpha_M \sin^2 \frac{\tilde{\omega}nd}{2} \right), \quad (17)$$

where t is the transmission coefficient and $T = |t|^2$ gives the transmittance. Similarly, the backward-propagating reflected light from the bilayer at a distance $z \ll -d/2$ is given by

$$E_{\text{backward}}(z) = \frac{i\tilde{\omega}}{2\epsilon_0 n} e^{-i\tilde{\omega}nz} (P_1 e^{-i\tilde{\omega}nd/2} + P_2 e^{i\tilde{\omega}nd/2}). \quad (18)$$

Following a simplification procedure similar to that used in deriving (17), we can write

$$r \equiv \frac{E_{\text{backward}}(z)}{E_{\text{inc}} e^{-i\tilde{\omega}nz}} = \frac{i\tilde{\omega}n}{a^2} \left(\alpha_A \cos^2 \frac{\tilde{\omega}nd}{2} - \alpha_M \sin^2 \frac{\tilde{\omega}nd}{2} \right), \quad (19)$$

where r is the reflection coefficient and the reflectance $R = |r|^2$. The absorption is then given by $A = 1 - R - T$.

Figures 3(a) and 3(d) show the absorption spectra of perfectly aligned bilayers ($\Delta = 0$), with relative separations d/a of 0.4 and 0.6, respectively. For both bilayers, there is a narrow absorption peak around 215 THz that, as we discuss later, corresponds to the resonance of the dark M mode. Including the $T_{xx}(\mathbf{0}, d)$ terms in the analytical model redshifts this absorption peak and results in better agreement between the analytically calculated spectra and the FDTD simulations. The dip in the reflectance spectrum, shown in Figs. 3(b) and 3(e), occurs at the spectral overlap of the bright A mode and the

dark M mode. The reflectance spectrum is largely flat between this dip and 320 THz, with an average reflectance of 80%, and essentially forms a stop band. The broad absorption resonance of the A mode can be observed in the analytical spectra beyond 350 THz and blueshifts as d is reduced. In the FDTD result, an additional absorption peak around 320 THz is due to the electric quadrupolar mode of the nanoantenna (see Appendix A) and overshadows the absorption peak of the A mode for both bilayers. Ignoring this multipolar contribution at frequencies larger than 320 THz, our dipolar analytical model is able to largely reproduce the results from the full-wave FDTD simulations with a reasonable accuracy.

Figures 3(c) and 3(f) show the spectra of P_A (solid lines) and P_M (dot-dashed lines) of the two bilayers without and with the absorption losses, respectively. The polarization spectra of a single nanoantenna array P_{eff} (black dashed lines) without and with the absorption losses are shown in the respective panels. The absorption losses are excluded by replacing $\alpha_{\text{shift}}^{-1}$ with $\text{Re}[\alpha_{\text{shift}}^{-1}]$ in (6), which, as observed in Fig. 3(c), leads to narrower resonances throughout. However, for a single array the collective radiation reaction of the array is significantly larger than the absorption losses. Hence, ignoring the absorption losses leads to a barely perceptible narrowing of the spectrum of P_{eff} . For the bilayer, the P_A and P_M modes have equal and opposite resonance shifts with respect to the resonance of P_{eff} . The resonance linewidth of (dark) P_M is also much narrower than that of (bright) P_A , and P_M is significantly larger than both P_A and P_{eff} at its resonance even with the absorption losses. Figure 4 shows the normalized field polarization ($P_x = \epsilon_0 \epsilon_r E_x / a^2$) at the resonances of the A (top) and

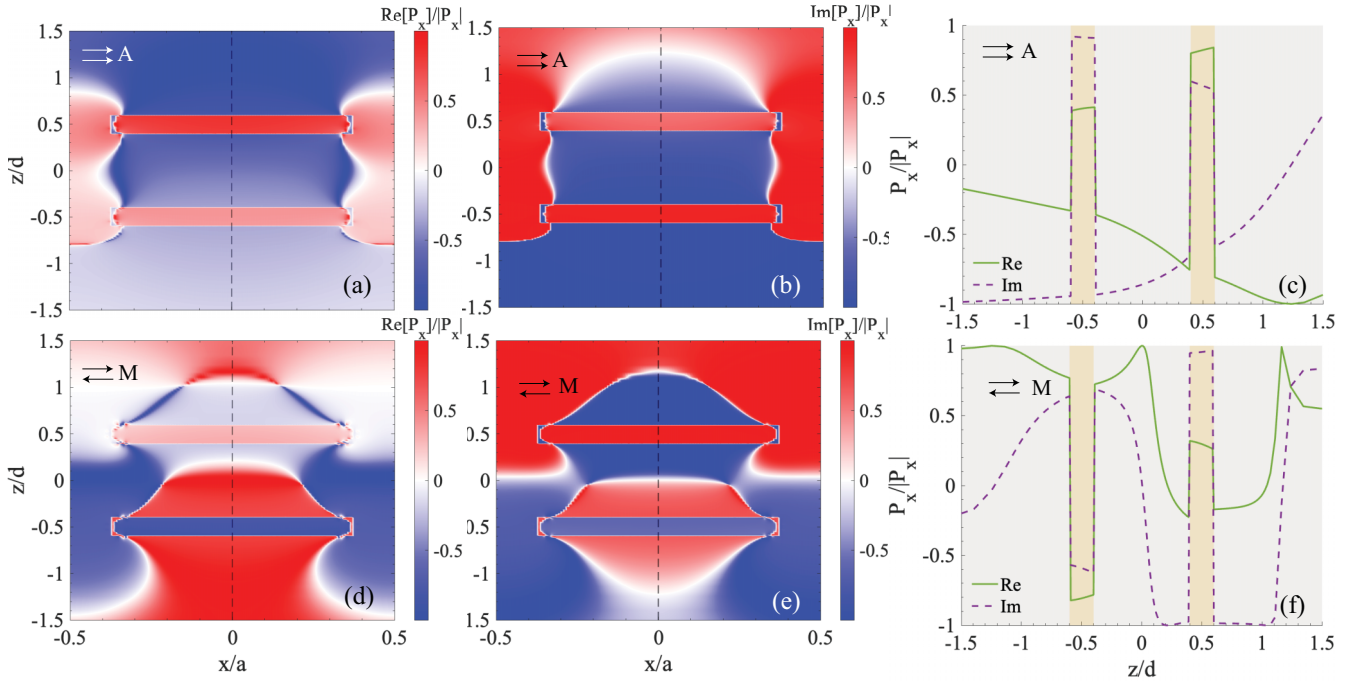


FIG. 4. Normalized real (left panels) and imaginary (middle panels) parts of the field polarization $P_x(x, z) = \epsilon_0 \epsilon_r(x, z) E_x(x, z) / a^2$ in a single unit cell of a bilayer structure with $d/a = 0.4$ in the xz plane. The field distribution E_x is obtained from FDTD simulations, and ϵ_r is the relative permittivity of the medium at a point (x, z) . The top (bottom) panels show the polarization distributions at the resonance of the A (M) mode. The panels on the right show linecuts of the respective modes along the z axis (black dotted lines in the left and middle panels), $P_x(0, z) / |P_x(0, z)|$. The yellow shaded regions represent the z locations of the nanoantennas.

M (bottom) modes in the xz plane of a single unit cell of the bilayer with $d/a = 0.4$. Here, ϵ_r is the relative permittivity at a given location, and E_x is the local field obtained from FDTD simulations. Consistent with our predictions, we observe that for the A (M) mode, P_x within both nanoantennas have the same (opposite) phase. The large field enhancements at the corners of the nanoantennas are due to the large field gradient at these metallic corners, also known as the “lightning rod” effect [46,47].

We now consider the effect of misalignments between the layers, which is a typical fabrication error in multilayered metasurfaces. Figure 5 compares the reflectance spectra of bilayers without [Fig. 5(a)] and with [Fig. 5(b)] misalignments ($\{\Delta_x, \Delta_y\} = \{0.2a, 0.2a\}$) for various separations d/a between the layers indicated in the legend. The solid lines are the reflectance spectra obtained from the analytical model, while the dashed lines are obtained from FDTD simulations. We note that the positions of the reflectance dip in the simulated and analytically calculated spectra for both perfectly aligned and misaligned structures agree reasonably well with an accuracy larger than 95%. Additionally, the effect of misalignments becomes more pronounced as the separation between the layers is reduced. This effect is not surprising, as the $T_{xx}(\Delta, d)$ terms that lead to retardation induced resonance shifts in both P_A and P_M get larger as d is reduced and are sensitive to lattice misalignments. For the smallest separation considered here, this misalignment-induced resonance shift is as large as 12 THz (or about 75 nm). Hence, along with d and a , the lattice misalignments $\{\Delta_x, \Delta_y\}$ are another set of parameters that can be used for designing broadband spectral filters.

III. COHERENT PERFECT ABSORPTION

Our analysis so far has been restricted to a single incident field on the bilayers, which behaves as a one port system. We now consider the situation in which the bilayers are excited by two counterpropagating fields $E_1 e^{i(\tilde{\omega}nz - \omega t)} \hat{x}$ and $E_2 e^{-i(\tilde{\omega}nz + \omega t)} \hat{x}$, which is essentially a two-port scenario. Both the phases and the amplitudes of the incident fields $E_{1,2}$ now constitute another set of parameters for the coherent control of scattering and absorption of light [40,41,48,49]. We note that even with misalignments, the bilayers are symmetric with respect to the direction of excitation under normal incidence, which is also evident in the relation $T_{xx}(\Delta, d) = T_{xx}(-\Delta, -d)$. Accordingly, we define a 2×2 symmetric scattering matrix S_{scat} that relates the vector of incoming fields $[E_2, E_1]^T$ to the outgoing fields $[E_2^-, E_1^-]^T$ as

$$\begin{bmatrix} E_2^- \\ E_1^- \end{bmatrix} = S_{\text{scat}} \begin{bmatrix} E_2 \\ E_1 \end{bmatrix} = \begin{bmatrix} r & t \\ t & r \end{bmatrix} \begin{bmatrix} E_2 \\ E_1 \end{bmatrix}, \quad (20)$$

where r and t are the transmission and reflection coefficients defined in (17) and (19), respectively.

For the specific set of input fields where there are no outgoing fields, i.e., $[E_2^-, E_1^-]^T$ is a null vector, the incoming radiation is converted to trapped radiation that dissipates non-radiatively within the system. This effect has been referred to as coherent perfect absorption (CPA) and is the time-reversed counterpart of laser action [40,41,49]. Setting $[E_2^-, E_1^-]^T$ to a null vector in (20) leads to the condition that for a non-trivial solution of (20) to exist, $|\det(S_{\text{scat}})|$ must approach zero, or $|r^2 - t^2| \approx 0$. The symmetric solution $(r + t) \approx 0$

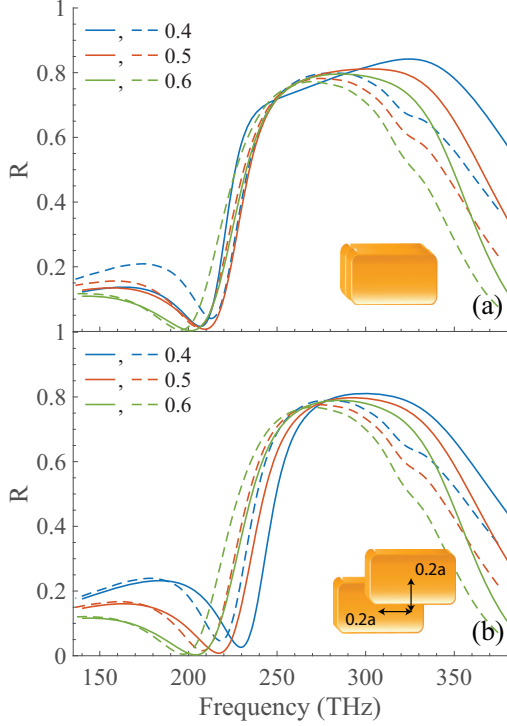


FIG. 5. Reflectance spectra of (a) perfectly aligned and (b) misaligned bilayers with $\{\Delta_x, \Delta_y\} = \{0.2a, 0.2a\}$ with various separations d/a shown in the legend. The solid reflectance curves were calculated using the full analytical model with the near-field terms $T_{xx}(0.2a, 0.2a, d)$, and the dashed curves were obtained from FDTD simulations.

corresponds to the eigenvector $[E_2, E_1]^T = [1, 1]^T$, which implies that the CPA condition is satisfied when $E_2 = E_1$. Similarly, the antisymmetric solution $(r - t) \approx 0$ corresponds to the eigenvector $[E_2, E_1]^T = [1, -1]^T$, or the CPA condition is satisfied when $E_2 = -E_1$. We also note that it is not possible to satisfy either of the CPA conditions with a single array of dipolar nanoparticles that is not backed by a reflector [50].

From (17) and (19), we write the antisymmetric CPA condition as

$$r - t = -\left(1 + \frac{2i\tilde{\omega}}{a^2}\alpha_M \sin^2 \frac{\tilde{\omega}nd}{2}\right) = 0, \quad (21)$$

which, with the use of (14), simplifies to

$$\alpha_{\text{shift}}^{-1} - S + \frac{i\tilde{\omega}}{a^2} \sin^2 \frac{\tilde{\omega}nd}{2} = 0. \quad (22)$$

At the resonance of the M mode, $\text{Re}[\alpha_{\text{shift}}^{-1}] - S = 0$. Recalling that $\text{Im}[\alpha_{\text{shift}}^{-1}] = \text{Im}[\alpha_0^{-1}]$ and that $\text{Im}[\alpha_0^{-1}] (= -\text{Im}[\alpha_0]/|\alpha_0|^2)$ is negative, we get the following simplified antisymmetric CPA condition at the resonance of the M mode:

$$|\text{Im}[\alpha_0^{-1}]| = \frac{n\tilde{\omega}}{a^2} \sin^2 \frac{\tilde{\omega}nd}{2}. \quad (23)$$

Similarly, the simplified symmetric CPA condition at the resonance of the A mode can be written as

$$|\text{Im}[\alpha_0^{-1}]| = \frac{n\tilde{\omega}}{a^2} \cos^2 \frac{\tilde{\omega}nd}{2}. \quad (24)$$

The CPA conditions (23) and (24) can also be interpreted as critical coupling conditions to the M and A modes of the bilayer, respectively, wherein the absorption losses are balanced by radiative coupling losses to the respective mode. For very small separations between the bilayers, such that $\tilde{\omega}nd \ll 1$, the right-hand side of (23) becomes proportional to $(d/a)^2$, while the right-hand side of (24) becomes proportional to $1/a^2$. For the nanoantenna arrays with significantly larger collective radiation reaction than absorption, it is straightforward to see that the antisymmetric, and not the symmetric, CPA condition (23) should hold true when $\tilde{\omega}nd \ll 1$. Figure 6(a) shows the spectra of $|\det(S_{\text{scat}})|$ for various separations d/a of perfectly aligned bilayers. The minima, indicated by the blue regions in the plot, indicate the separations d/a where the CPA conditions are satisfied for a particular range of frequencies. The black (white) contours identify the antisymmetric (symmetric) sets of CPA solutions. We note that the variation of $|\det(S_{\text{scat}})|$ shown in Fig. 6(a) is very similar to the variation of the absorption spectra of a perfect absorber consisting of a single dipolar metasurface backed by a reflector [50].

As a metric for CPA, we define the joint absorption \mathcal{A} [41] as follows:

$$\mathcal{A} = 1 - \frac{|E_1^-|^2 + |E_2^-|^2}{|E_1|^2 + |E_2|^2}. \quad (25)$$

Specifically, for equal-amplitude fields with a phase difference of ϕ , or $E_2 = E_1 e^{i\phi}$, from (20) we get, after some simplification,

$$\mathcal{A} = 1 - |r|^2 - |t|^2 - (r^*t + rt^*) \cos \phi. \quad (26)$$

The spectra of \mathcal{A} for symmetric ($\phi = 0$, solid blue lines) and antisymmetric ($\phi = \pi$ rad, solid red lines) excitations and the absorption spectrum A for a single incident field (dashed black lines) are shown in Figs. 6(b) and 6(c) for two perfectly aligned bilayers with separations d/a of 0.34 and 1.08, respectively. As shown in Fig. 6(a), the separation d/a of 0.34 (1.08) satisfies the antisymmetric (symmetric) CPA condition. Accordingly, the joint absorption \mathcal{A} in Fig. 6(b) approaches unity for antisymmetric excitation (red) at the resonance of the M mode and is significantly smaller than the absorption A for a single incident field around the resonance of the A mode. On the other hand, \mathcal{A} under symmetric excitation (blue) is almost twice the absorption A for single-field excitation around the resonance of the A mode and is significantly smaller than the corresponding single-field absorption around the resonance of the M mode. The opposite trend holds true for the bilayer that satisfies the symmetric CPA conditions shown in Fig. 6(c) as the symmetric (antisymmetric) mode becomes the dark (bright) mode for this bilayer.

Thus, the excitation by two counterpropagating fields of equal intensity is a way of mode matching the incident fields to either the bright mode or the dark mode by adjusting the relative phase of the fields. Figure 6(d) shows the variation with respect to the relative phase ϕ of \mathcal{A} at the single-field absorption resonance frequency of the two bilayers shown in Figs. 6(b) (blue solid line) and 6(c), respectively. The maximum variation in \mathcal{A} achievable at the CPA condition is given by the magnitude of the difference in \mathcal{A} for in-phase ($\phi = 0$) and out-of-phase ($\phi = \pi$) excitation after substituting

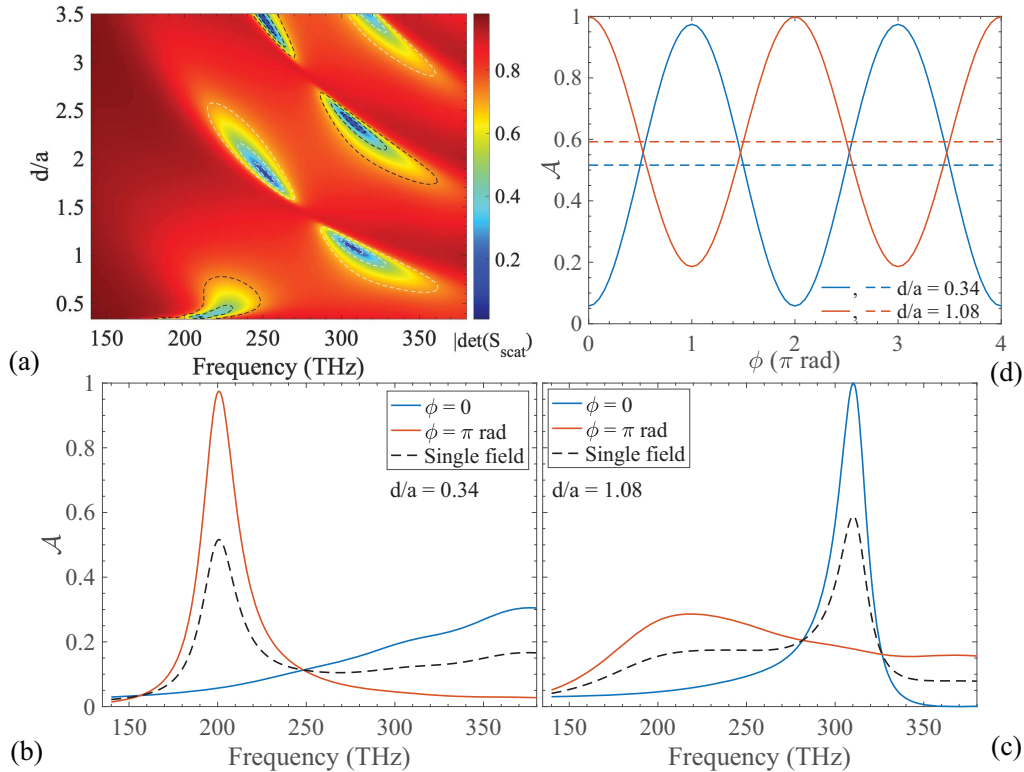


FIG. 6. (a) Spectra of $|\det(S_{\text{scat}})|$ for various separations d of perfectly aligned bilayers. Absorption spectra of a bilayer with (b) $d/a = 0.34$ and (c) $d/a = 1.08$ for a single normally incident field (black dashed lines) and two counterpropagating normally incident fields with equal amplitude and the same phase (blue lines) and opposite phases (red lines). (d) The joint absorption \mathcal{A} as the phase difference ϕ between the two fields $E_{1,2}$ is varied (solid lines) for bilayers with $d/a = 0.34$ (blue lines) and $d/a = 1.08$ (red lines). The respective maximum single-incident-field absorption values are shown by dashed lines.

the CPA conditions $r = \pm t$ in Eq. (26). After some simplification, we find that the maximum achievable variation in \mathcal{A} is approximately $4R$, with R being the reflectance of the bilayer for a single incident field. We observe a variation in \mathcal{A} as large as 0.9 for $d/a = 0.34$ and 0.82 for $d/a = 1.08$ at the respective CPA frequency. These estimated values of the variation in \mathcal{A} are close to the values of $4R$ for the respective bilayers with a single-field excitation. This property makes these bilayers useful for applications in all-optical modulation and switching without the need for any optical nonlinearity. The relative phase-dependent absorption also implies that the bilayer essentially behaves as an absorptive interferometer at the CPA point and has applications in areas such as pattern recognition [51,52].

IV. CONCLUSIONS

To summarize, we have studied the formation of dark and bright modes in a system of two dipolar nanoantenna arrays separated by a subwavelength distance, using a simple analytical model based on the point-dipole approximation as well as full-wave FDTD simulations; the approximate point-dipole model can be used to explore the response of the system over a wide frequency range. We have discussed how the radiative coupling between the layers leads to resonance shifts as well as linewidth variations, wherein the bright (dark) mode has a larger (smaller) radiative damping than the single layer.

Our analytical model also accounts for near-field interactions between the two arrays and can model the scattering and absorption behavior of the bilayer structure with reasonable accuracy, including the effects of misalignments between the two layers. The dark mode can make a significant contribution to the optical response of the system. Finally, we have shown that these dark and bright modes can be selectively excited through two equal-intensity counterpropagating fields by varying the relative phase between them. And so the scattering and absorption behavior of these bilayers can be coherently controlled.

We note that the choice of materials and the geometrical parameters of our system have been motivated by our in-house fabrication capabilities and our previous successful demonstration of a single nanoantenna array [29]. However, our model can be extended to various combinations of plasmonic as well as dielectric materials and substrates, as well as to different nanoparticle shapes and sizes, and can be used to design devices such as spectral filters, optical switches, and modulators in the spectral range of choice. The large local-field enhancement for the dark modes can also be used to enhance nonlinear interactions when integrated with epsilon-near-zero materials [53]. Last, this analytical model can be extended to multilayered structures and can be used to calculate the effective-medium parameters of these metacrystals, which we will discuss in our followup work.

ACKNOWLEDGMENTS

The portion of the work performed at the University of Toronto was supported by the Natural Sciences and Engineering Research Council of Canada under Discovery Grant No. RGPIN2019-04170. The portion of the work performed at the University of Rochester was supported by the US Defense Advanced Research Projects Agency Award No. W911NF-18-1-0369, US Army Research Office Award No. W911NF-18-1-0337, the US Office of Naval Research Award No. N00014-19-1-2247 and MURI Award No. N00014-20-1-2558, the US National Science Foundation Award No. 2138174, and the Department of Energy Award No. FWP 76295. The portion of the work performed at the University of Ottawa was supported by the Canada Research Chairs program under Award No. 950-231657, the Natural Sciences and Engineering Research Council of Canada under Discovery Grant No. RGPIN/2017-06880, and the Canada First Research Excellence Fund Award No. 072623.

APPENDIX A: SINGLE NANOANTENNA SCATTERING AND EXTINCTION PROPERTIES

To calculate the dipolar polarizability, and hence the scattering, absorption, and extinction cross sections of a single nanoantenna in the point-dipole approximation, we use the same method as described in Appendix B of our earlier work [29]. Figures 7(a), 7(b) and 7(c) compare the spectra of the scattering, absorption, and extinction cross sections, respectively, of the nanoantenna obtained from FDTD (blue dot-dashed lines) and from the analytical model. The resonant scattering cross section of an individual nanoantenna is almost three times the resonant absorption. We see that the simulated and calculated extinction and absorption cross-section spectra agree reasonably well. For the absorption spectrum, however, additional features are present at frequencies higher than the absorption resonance for the FDTD result but not for the analytically calculated result. These additional features are due to the multipolar contributions, with the prominent bump around 350 THz due to the electric quadrupolar component. Obviously, these contributions are not accounted for in our dipolar analytical model, and hence, they contribute to the disagreement between the analytically calculated and simulated spectra for the bilayers in the frequency range 280–380 THz.

APPENDIX B: ELECTRIC FIELD FROM A TWO-DIMENSIONAL LATTICE OF IDENTICAL ELECTRIC DIPOLES

Here, we present the derivation of (8), which is the electric field at a given point in space from a square lattice of identical electric dipoles of dipole moment \mathbf{p} located in the xy plane. We consider fields at a fixed frequency ω , or

$$\mathbf{E}(\mathbf{r}, t) = \mathbf{E}(\mathbf{r})e^{-i\omega t} + \text{c.c.}, \quad (\text{B1})$$

and assuming a source polarization $\mathbf{P}(\mathbf{r})$ in a background medium of refractive index n , we have [54]

$$\mathbf{P}(\mathbf{R}; z) = \int \frac{d\boldsymbol{\kappa}}{(2\pi)^2} \mathbf{P}(\boldsymbol{\kappa}; z) e^{i\boldsymbol{\kappa} \cdot \mathbf{R}}, \quad (\text{B2})$$

$$\mathbf{E}(\mathbf{R}; z) = \int \frac{d\boldsymbol{\kappa}}{(2\pi)^2} \mathbf{E}(\boldsymbol{\kappa}; z) e^{i\boldsymbol{\kappa} \cdot \mathbf{R}}, \quad (\text{B3})$$

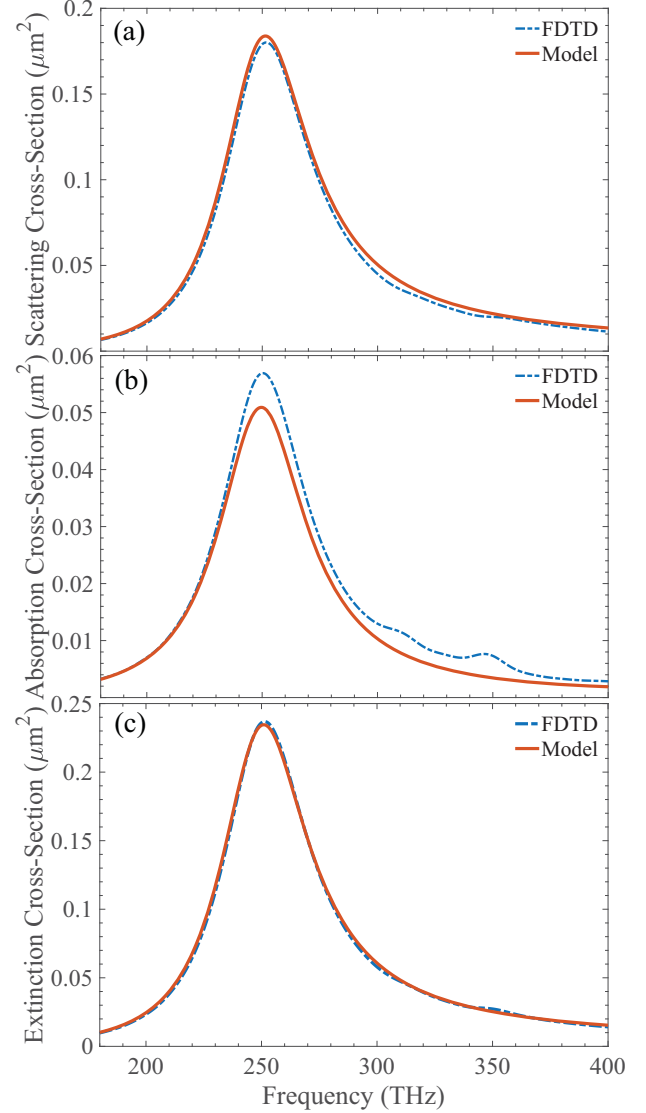


FIG. 7. (a) Scattering, (b) absorption, and (c) extinction cross-section spectra of an individual nanoantenna obtained from FDTD simulations (blue dot-dashed lines) and from the dipolar analytical model (red solid lines).

where $\mathbf{P}(\mathbf{r}) = \mathbf{P}(\mathbf{R}; z)$, $\boldsymbol{\kappa} = (\kappa_x, \kappa_y)$, and

$$\mathbf{E}(\boldsymbol{\kappa}; z) = \int \mathbf{G}(\boldsymbol{\kappa}; z - z') \cdot \mathbf{P}(\boldsymbol{\kappa}; z') dz', \quad (\text{B4})$$

with $\mathbf{G}(\boldsymbol{\kappa}; z)$ being the Green's function, given by

$$\begin{aligned} \mathbf{G}(\boldsymbol{\kappa}; z) = & \frac{i\tilde{\omega}^2}{2\epsilon_0 w} (\hat{\delta}\hat{\delta} + \hat{\mathbf{p}}_+ \hat{\mathbf{p}}_+) \theta(z - z') e^{i w(z - z')} \\ & + \frac{i\tilde{\omega}^2}{2\epsilon_0 w} (\hat{\delta}\hat{\delta} + \hat{\mathbf{p}}_- \hat{\mathbf{p}}_-) \theta(z' - z) e^{-i w(z - z')} \\ & - \frac{\hat{\mathbf{z}}\hat{\mathbf{z}}}{2\epsilon_0 n^2} \delta(z - z'). \end{aligned} \quad (\text{B5})$$

Here, $\theta(z)$ is the Heaviside step function,

$$w = \sqrt{\tilde{\omega}^2 n^2 - \kappa^2},$$

and

$$\begin{aligned}\hat{s} &= \hat{\kappa} \times \hat{z}, \\ \hat{p}_{\pm} &= \frac{\kappa \hat{z} \mp w \hat{\kappa}}{\tilde{\omega} n},\end{aligned}$$

with $\kappa = |\kappa|$. We assume the lattice positions of the nanoantenna array are

$$\mathbf{R}_l = l_x a \hat{x} + l_y a \hat{y},$$

with a being the lattice constant; l denotes (l_x, l_y) , where l_x and l_y are integers. The reciprocal lattice vectors are then given by

$$\mathbf{K}_m = \frac{2\pi}{a} m_x \hat{x} + \frac{2\pi}{a} m_y \hat{y}, \quad (\text{B6})$$

where m denotes (m_x, m_y) , with m_x and m_y being integers. The relation $e^{i\mathbf{K}_m \cdot \mathbf{R}_l} = 1$ holds for any \mathbf{R}_l and any \mathbf{K}_m

In the point-dipole approximation, the polarizations $\mathbf{P}(\mathbf{R}; z)$ and $\mathbf{P}(\kappa; z)$ of the plane of dipoles can be written as

$$\mathbf{P}(\mathbf{R}; z) = \delta(z) \sum_l \mathbf{p} \delta(\mathbf{R} - \mathbf{R}_l), \quad (\text{B7})$$

$$\mathbf{P}(\kappa; z) = \delta(z) \mathbf{p} \sum_l e^{-i\kappa \cdot \mathbf{R}_l}. \quad (\text{B8})$$

Substituting (B8) in (B4), we get, after some simplification,

$$\mathbf{E}(\kappa; z) = \frac{i\tilde{\omega}^2}{2\epsilon_0 w} (\hat{s} \hat{s} + \hat{p}_{\pm} \hat{p}_{\pm}) \cdot \mathbf{p} \sum_l e^{-i\kappa \cdot \mathbf{R}_l} e^{i w |z|}. \quad (\text{B9})$$

Then using (B9) and (B3), we get

$$\begin{aligned}\mathbf{E}(\mathbf{R}; z) &= \frac{i\tilde{\omega}^2}{2\epsilon_0} \int \frac{d\kappa}{(2\pi)^2 w} (\hat{s} \hat{s} + \hat{p}_{\pm} \hat{p}_{\pm}) \cdot \mathbf{p} \\ &\times \left(\sum_l e^{i\kappa \cdot (\mathbf{R} - \mathbf{R}_l)} \right) e^{i w |z|}.\end{aligned} \quad (\text{B10})$$

We now set $\mathbf{R} = \mathbf{R}_j + \mathbf{\Delta}$, where \mathbf{R}_j is some lattice site and $\mathbf{\Delta}$ is the displacement from the lattice site; using the lattice property $e^{i\kappa \cdot (\mathbf{R}_j - \mathbf{R}_l)} = 1$, we get

$$\begin{aligned}\mathbf{E}(\mathbf{R}; z) &= \frac{i\tilde{\omega}^2}{2\epsilon_0} \int \frac{e^{i\kappa \cdot \mathbf{\Delta}} d\kappa}{(2\pi)^2 w} (\hat{s} \hat{s} + \hat{p}_{\pm} \hat{p}_{\pm}) \cdot \mathbf{p} \\ &\times \left(\sum_l e^{i\kappa \cdot \mathbf{R}_l} \right) e^{i w |z|}.\end{aligned} \quad (\text{B11})$$

We then use the standard lattice result

$$\frac{a^2}{(2\pi)^2} \sum_l e^{i\kappa \cdot \mathbf{R}_l} = \sum_m \delta(\kappa - \mathbf{K}_m)$$

in (B11) to get

$$\mathbf{E}(\mathbf{R}_j + \mathbf{\Delta}; z) = \frac{i\tilde{\omega}^2}{2\epsilon_0 a^2} \sum_m \frac{e^{i\mathbf{K}_m \cdot \mathbf{\Delta}}}{w} (\hat{s} \hat{s} + \hat{p}_{\pm} \hat{p}_{\pm}) \cdot \mathbf{p} e^{i w |z|}, \quad (\text{B12})$$

where w , \hat{s} , and \hat{p}_{\pm} are now functions of \mathbf{K}_m given by

$$\begin{aligned}\hat{s} &= \hat{\mathbf{K}}_m \times \hat{z}, \\ \hat{p}_{\pm} &= \frac{K_m \hat{z} \mp w(K_m) \hat{\mathbf{K}}_m}{\tilde{\omega} n},\end{aligned}$$

$$w = \sqrt{\tilde{\omega}^2 n^2 - K_m^2}.$$

For $m = (0, 0)$, $w \rightarrow \tilde{\omega} n$, $K_{0,0} = 0$, and $\hat{\mathbf{K}}_{0,0}$ is poorly defined in this limit. However, regardless of the choice of unit vector for $\hat{\mathbf{K}}_{0,0}$, we have the condition

$$\hat{s} \hat{s} + \hat{p}_{\pm} \hat{p}_{\pm} \rightarrow \hat{x} \hat{x} + \hat{y} \hat{y},$$

which gives us the $m = (0, 0)$ field component as

$$[\mathbf{E}(\mathbf{R}_j + \mathbf{\Delta}; z)]_{m=(0,0)} = \frac{i\tilde{\omega}}{2\epsilon_0 a^2 n} (\hat{x} \hat{x} + \hat{y} \hat{y}) \cdot \mathbf{p} e^{i\tilde{\omega} n |z|}. \quad (\text{B13})$$

This is independent of displacement $\mathbf{\Delta}$ and has the form of a plane wave with no fast-decaying components. Hence, this $m = (0, 0)$ component is the radiative field contribution. For a small enough lattice constant a , the remaining terms in the sum in (B12) form the nonradiative contribution,

$$\begin{aligned}\mathbf{E}_{\text{nr}}(\mathbf{R}_j + \mathbf{\Delta}; z) &= \sum_{m \neq (0,0)} e^{i\mathbf{K}_m \cdot \mathbf{\Delta}} \left[\frac{i\tilde{\omega}^2}{2\epsilon_0 a^2 w} (\hat{s} \hat{s} + \hat{p}_{\pm} \hat{p}_{\pm}) \right] \cdot \mathbf{p} e^{i w |z|}.\end{aligned} \quad (\text{B14})$$

The nonradiative field

Assuming that the lattice constant a is small enough that for $(m_x, m_y) \neq (0, 0)$ we have purely imaginary w , we set

$$w = i q, \quad (\text{B15})$$

where $q = \sqrt{K_m^2 - \tilde{\omega}^2 n^2}$, which can be written in terms of the indices (m_x, m_y) as

$$q = \frac{2\pi}{a} \sqrt{(m_x^2 + m_y^2) - \frac{\tilde{\omega}^2 n^2 a^2}{(2\pi)^2}}. \quad (\text{B16})$$

We now define

$$\frac{\tilde{\omega} n a}{2\pi} = \eta, \quad (\text{B17})$$

and we can write

$$\frac{K_m}{\tilde{\omega} n} = \frac{2\pi}{\tilde{\omega} n a} \sqrt{m_x^2 + m_y^2} = \frac{D_m}{\eta}, \quad (\text{B18})$$

where $D_m = \sqrt{m_x^2 + m_y^2}$. For the subwavelength lattice constants assumed here, where for $(m_x, m_y) \neq (0, 0)$ we have q real, $\eta < 1$, and we can write

$$\frac{w}{i\tilde{\omega} n} = \frac{q}{\tilde{\omega} n} = \frac{1}{\eta} \sqrt{(m_x^2 + m_y^2) - \eta^2},$$

which simplifies to

$$\frac{q}{\tilde{\omega} n} = \frac{1}{\eta} \sqrt{D_m^2 - \eta^2} = \frac{D_m \gamma_m}{\eta}, \quad (\text{B19})$$

where

$$\gamma_m = \sqrt{1 - \frac{\eta^2}{D_m^2}}$$

and is always real and slightly less than unity for $\eta < 1$. We now simplify the prefactor of the unit dyadics in (B14) as

$$\frac{i\tilde{\omega}^2}{2\epsilon_0 a^2 w} = \frac{\tilde{\omega}}{2\epsilon_0 a^2 n} \frac{\tilde{\omega} n}{q} = \frac{\pi}{\epsilon_0 a^3 n^2} \frac{\eta^2}{D_m \gamma_m}. \quad (\text{B20})$$

The propagator $e^{i\omega|z|}$, which we define as $f_m(|z|)$, can also be simplified to

$$f_m(|z|) = e^{-q|z|} = e^{-\frac{\omega}{\eta} D_m \gamma_m |z|} = e^{-2\pi D_m \gamma_m \frac{|z|}{a}}. \quad (\text{B21})$$

We also define

$$\Phi(\Delta) = \mathbf{K}_m \cdot \Delta = 2\pi \left(m_x \frac{\Delta_x}{a} + m_y \frac{\Delta_y}{a} \right). \quad (\text{B22})$$

Substituting Eqs. (B20)–(B22) in (B14), we get

$$\begin{aligned} \mathbf{E}_{\text{nrad}}(\mathbf{R}_j + \Delta; z) &= \frac{\pi}{\epsilon_0 a^3 n^2} \sum_{m \neq (0,0)} e^{i\Phi_m(\Delta)} f_m(|z|) \\ &\times \left[\frac{\eta^2}{D_m \gamma_m} (\hat{s}\hat{s} + \hat{p}_\pm \hat{p}_\pm) \right] \cdot \mathbf{p}. \end{aligned} \quad (\text{B23})$$

We now simplify the unit dyadics in (B23) in terms of the cartesian vectors. So we have

$$\begin{aligned} \hat{\mathbf{K}}_m &= \frac{m_x \hat{\mathbf{x}} + m_y \hat{\mathbf{y}}}{D_m}, \\ \hat{\mathbf{s}} &= \hat{\mathbf{K}}_m \times \hat{\mathbf{z}} = \frac{-m_x \hat{\mathbf{x}} + m_y \hat{\mathbf{y}}}{D_m}. \end{aligned}$$

Hence, we write

$$\hat{s}\hat{s} = \frac{m_y^2 \hat{\mathbf{x}}\hat{\mathbf{x}} + m_x^2 \hat{\mathbf{y}}\hat{\mathbf{y}} - m_x m_y (\hat{\mathbf{x}}\hat{\mathbf{y}} + \hat{\mathbf{y}}\hat{\mathbf{x}})}{D_m^2} \quad (\text{B24})$$

and

$$\begin{aligned} \hat{p}_\pm \hat{p}_\pm &= \frac{K_m \hat{\mathbf{z}} \mp \omega \hat{\mathbf{K}}_m}{\tilde{\omega} n} \frac{K_m \hat{\mathbf{z}} \mp \omega \hat{\mathbf{K}}_m}{\tilde{\omega} n} \\ &= \frac{K_m^2}{\tilde{\omega}^2 n^2} \hat{\mathbf{z}}\hat{\mathbf{z}} - \frac{q^2}{\tilde{\omega}^2 n^2} \hat{\mathbf{K}}_m \hat{\mathbf{K}}_m \mp i \frac{K_m q}{\tilde{\omega}^2 n^2} (\hat{\mathbf{z}} \hat{\mathbf{K}}_m + \hat{\mathbf{K}}_m \hat{\mathbf{z}}), \end{aligned} \quad (\text{B25})$$

where we have used (B15) for simplification. We use (B18) and (B19) to further simplify Eq. (B25) above as

$$\hat{p}_\pm \hat{p}_\pm = \frac{D_m^2}{\eta^2} \hat{\mathbf{z}}\hat{\mathbf{z}} - \frac{D_m^2 \gamma_m^2}{\eta^2} \hat{\mathbf{K}}_m \hat{\mathbf{K}}_m \mp i \frac{D_m^2 \gamma_m}{\eta^2} (\hat{\mathbf{z}} \hat{\mathbf{K}}_m + \hat{\mathbf{K}}_m \hat{\mathbf{z}}). \quad (\text{B26})$$

We now simplify the second and third unit dyadics on the right-hand side of (B26). For the second unit dyadic, we have

$$\begin{aligned} \hat{\mathbf{K}}_m \hat{\mathbf{K}}_m &= \frac{m_x \hat{\mathbf{x}} + m_y \hat{\mathbf{y}}}{D_m} \frac{m_x \hat{\mathbf{x}} + m_y \hat{\mathbf{y}}}{D_m} \\ &= \frac{m_x^2 \hat{\mathbf{x}}\hat{\mathbf{x}} + m_y^2 \hat{\mathbf{y}}\hat{\mathbf{y}} + m_x m_y (\hat{\mathbf{x}}\hat{\mathbf{y}} + \hat{\mathbf{y}}\hat{\mathbf{x}})}{D_m^2}. \end{aligned} \quad (\text{B27})$$

The third unit dyadic in (B26) can be written as

$$\begin{aligned} \hat{\mathbf{z}} \hat{\mathbf{K}}_m + \hat{\mathbf{K}}_m \hat{\mathbf{z}} &= \hat{\mathbf{z}} \frac{m_x \hat{\mathbf{x}} + m_y \hat{\mathbf{y}}}{D_m} + \frac{m_x \hat{\mathbf{x}} + m_y \hat{\mathbf{y}}}{D_m} \hat{\mathbf{z}} \\ &= \frac{m_x}{D_m} (\hat{\mathbf{z}}\hat{\mathbf{x}} + \hat{\mathbf{x}}\hat{\mathbf{z}}) + \frac{m_y}{D_m} (\hat{\mathbf{z}}\hat{\mathbf{y}} + \hat{\mathbf{y}}\hat{\mathbf{z}}). \end{aligned} \quad (\text{B28})$$

Substituting (B27) and (B28) in (B26), we get

$$\begin{aligned} \hat{p}_\pm \hat{p}_\pm &= -\frac{m_x^2 \gamma_m^2}{\eta^2} \hat{\mathbf{x}}\hat{\mathbf{x}} - \frac{m_y^2 \gamma_m^2}{\eta^2} \hat{\mathbf{y}}\hat{\mathbf{y}} + \frac{D_m^2}{\eta^2} \hat{\mathbf{z}}\hat{\mathbf{z}} \\ &\quad - \frac{m_x m_y \gamma_m^2}{\eta^2} (\hat{\mathbf{x}}\hat{\mathbf{y}} + \hat{\mathbf{y}}\hat{\mathbf{x}}) \mp i \frac{m_y D_m \gamma_m}{\eta^2} (\hat{\mathbf{z}}\hat{\mathbf{y}} + \hat{\mathbf{y}}\hat{\mathbf{z}}) \end{aligned}$$

$$\mp i \frac{m_x D_m \gamma_m}{\eta^2} (\hat{\mathbf{z}}\hat{\mathbf{x}} + \hat{\mathbf{x}}\hat{\mathbf{z}}). \quad (\text{B29})$$

From (B24) and (B29), we write

$$\begin{aligned} &\eta^2 (\hat{s}\hat{s} + \hat{p}_\pm \hat{p}_\pm) \\ &= \hat{\mathbf{x}}\hat{\mathbf{x}} \left(\frac{\eta^2 m_y^2}{D_m^2} - m_x^2 \gamma_m^2 \right) + \hat{\mathbf{y}}\hat{\mathbf{y}} \left(\frac{\eta^2 m_x^2}{D_m^2} - m_y^2 \gamma_m^2 \right) \\ &\quad + \hat{\mathbf{z}}\hat{\mathbf{z}} D_m^2 + (\hat{\mathbf{x}}\hat{\mathbf{y}} + \hat{\mathbf{y}}\hat{\mathbf{x}}) \left(-\frac{\eta^2 m_x m_y}{D_m^2} - m_x m_y \gamma_m^2 \right) \\ &\quad + (\hat{\mathbf{z}}\hat{\mathbf{y}} + \hat{\mathbf{y}}\hat{\mathbf{z}}) (\mp i m_y D_m \gamma_m) + (\hat{\mathbf{z}}\hat{\mathbf{x}} + \hat{\mathbf{x}}\hat{\mathbf{z}}) (\mp i m_x D_m \gamma_m). \end{aligned} \quad (\text{B30})$$

The coefficients of the unit dyadics in (B30) can be further simplified. So we have

$$\begin{aligned} \frac{\eta^2 m_y^2}{D_m^2} - m_x^2 \gamma_m^2 &= \frac{\eta^2 m_y^2 - m_x^2 (D_m^2 - \eta^2)}{D_m^2} \\ &= \eta^2 \frac{m_x^2 + m_y^2}{D_m^2} - m_x^2 = \eta^2 - m_x^2. \end{aligned}$$

Similarly,

$$\frac{\eta^2 m_x^2}{D_m^2} - m_y^2 \gamma_m^2 = \eta^2 - m_y^2,$$

and

$$\begin{aligned} -\frac{\eta^2 m_x m_y}{D_m^2} - m_x m_y \gamma_m^2 &= m_x m_y \left(\frac{-\eta^2 - \gamma_m^2 D_m^2}{D_m^2} \right) \\ &= m_x m_y \left(\frac{-\eta^2 - (D_m^2 - \eta^2)}{D_m^2} \right) \\ &= -m_x m_y. \end{aligned}$$

On making the above substitutions, Eq. (B30) becomes

$$\begin{aligned} &\eta^2 (\hat{s}\hat{s} + \hat{p}_\pm \hat{p}_\pm) \\ &= \hat{\mathbf{x}}\hat{\mathbf{x}} (\eta^2 - m_x^2) + \hat{\mathbf{y}}\hat{\mathbf{y}} (\eta^2 - m_y^2) + \hat{\mathbf{z}}\hat{\mathbf{z}} D_m^2 \\ &\quad + (\hat{\mathbf{x}}\hat{\mathbf{y}} + \hat{\mathbf{y}}\hat{\mathbf{x}}) (-m_x m_y) + (\hat{\mathbf{z}}\hat{\mathbf{y}} + \hat{\mathbf{y}}\hat{\mathbf{z}}) (\mp i m_y D_m \gamma_m) \\ &\quad + (\hat{\mathbf{z}}\hat{\mathbf{x}} + \hat{\mathbf{x}}\hat{\mathbf{z}}) (\mp i m_x D_m \gamma_m). \end{aligned} \quad (\text{B31})$$

Substituting (B31) in (B23), we can write

$$\mathbf{E}_{\text{nrad}}(\mathbf{R}_j + \Delta; z) = \frac{\pi}{\epsilon_0 a^3 n^2} \mathbf{T}(\Delta, z) \cdot \mathbf{p}, \quad (\text{B32})$$

where $\mathbf{T}(\Delta, z)$ is a dimensionless dyadic of the form

$$\begin{aligned} \mathbf{T}(\Delta, z) &= T_{xx}(\Delta, z) \hat{\mathbf{x}}\hat{\mathbf{x}} + T_{yy}(\Delta, z) \hat{\mathbf{y}}\hat{\mathbf{y}} + T_{zz}(\Delta, z) \hat{\mathbf{z}}\hat{\mathbf{z}} \\ &\quad + T_{xy}(\Delta, z) (\hat{\mathbf{x}}\hat{\mathbf{y}} + \hat{\mathbf{y}}\hat{\mathbf{x}}) + T_{yz}(\Delta, z) (\hat{\mathbf{z}}\hat{\mathbf{y}} + \hat{\mathbf{y}}\hat{\mathbf{z}}) \\ &\quad \times T_{zx}(\Delta, z) (\hat{\mathbf{x}}\hat{\mathbf{z}} + \hat{\mathbf{z}}\hat{\mathbf{x}}), \end{aligned}$$

with

$$\begin{aligned} T_{xx}(\Delta, z) &= \sum_{m \neq (0,0)} e^{i\Phi_m(\Delta)} f_m(|z|) \left(\frac{\eta^2 - m_x^2}{D_m \gamma_m} \right), \\ T_{yy}(\Delta, z) &= \sum_{m \neq (0,0)} e^{i\Phi_m(\Delta)} f_m(|z|) \left(\frac{\eta^2 - m_y^2}{D_m \gamma_m} \right), \end{aligned}$$

$$\begin{aligned}
T_{zz}(\mathbf{\Delta}, z) &= \sum_{m \neq (0,0)} e^{i\Phi_m(\Delta)} f_m(|z|) \left(\frac{D_m}{\gamma_m} \right), \\
T_{xy}(\mathbf{\Delta}, z) &= \sum_{m \neq (0,0)} e^{i\Phi_m(\Delta)} f_m(|z|) \left(-\frac{m_x m_y}{D_m \gamma_m} \right), \\
T_{yz}(\mathbf{\Delta}, z) &= \sum_{m \neq (0,0)} e^{i\Phi_m(\Delta)} f_m(|z|) (\mp i m_y), \\
T_{zx}(\mathbf{\Delta}, z) &= \sum_{m \neq (0,0)} e^{i\Phi_m(\Delta)} f_m(|z|) (\mp i m_x). \quad (\text{B33})
\end{aligned}$$

The tensor components given in (B33) can be further simplified by noting that

$$e^{i\Phi_m(\Delta)} = \cos[\Phi_m(\Delta)] + i \sin \cos[\Phi_m(\Delta)],$$

and we get

$$\begin{aligned}
T_{xx}(\mathbf{\Delta}, z) &= \sum_{m \neq (0,0)} f_m(|z|) \left(\frac{\eta^2 - m_x^2}{D_m \gamma_m} \right) \cos[\Phi_m(\Delta)], \\
T_{yy}(\mathbf{\Delta}, z) &= \sum_{m \neq (0,0)} f_m(|z|) \left(\frac{\eta^2 - m_y^2}{D_m \gamma_m} \right) \cos[\Phi_m(\Delta)], \\
T_{zz}(\mathbf{\Delta}, z) &= \sum_{m \neq (0,0)} f_m(|z|) \left(\frac{D_m}{\gamma_m} \right) \cos[\Phi_m(\Delta)],
\end{aligned}$$

$$\begin{aligned}
T_{xy}(\mathbf{\Delta}, z) &= \sum_{m \neq (0,0)} f_m(|z|) \left(-\frac{m_x m_y}{D_m \gamma_m} \right) \cos[\Phi_m(\Delta)], \\
T_{yz}(\mathbf{\Delta}, z) &= \text{sgn}(z) \sum_{m \neq (0,0)} f_m(|z|) m_y \sin[\Phi_m(\Delta)], \\
T_{zx}(\mathbf{\Delta}, z) &= \text{sgn}(z) \sum_{m \neq (0,0)} f_m(|z|) m_x \sin[\Phi_m(\Delta)]. \quad (\text{B34})
\end{aligned}$$

We note that all the tensor components given above are purely real, which is expected for $\mathbf{E}_{\text{nrad}}(\mathbf{R}_j + \mathbf{\Delta}; z)$ being a purely nonradiative field.

For all the dipoles aligned along $\hat{\mathbf{x}}$, which is the case for the nanoantenna array excited by a normally incident plane wave polarized along the dipole moments oriented along the x axis, only the $T_{xx}(\mathbf{\Delta}, z)$ tensor component is nonzero. Hence, the x -polarized electric field from the sheet of dipoles given by the Eqs. (B13) and (B32) is as follows:

$$E_x(\mathbf{R}_j + \mathbf{\Delta}; z) = \frac{i\tilde{\omega}}{2\epsilon_0 n} \frac{P_x}{a^2} e^{i\tilde{\omega}|z|} + \frac{\pi}{\epsilon_0 a n^2} T_{xx}(\mathbf{\Delta}, z) \frac{P_x}{a^2}. \quad (\text{B35})$$

-
- [1] E. Hutter and J. H. Fendler, *Adv. Mater.* **16**, 1685 (2004).
- [2] L. Novotny and B. Hecht, *Principles of Nano-optics* (Cambridge University Press, Cambridge, 2012).
- [3] W. Cai, U. K. Chettiar, A. V. Kildishev, and V. M. Shalaev, *Nat. Photonics* **1**, 224 (2007).
- [4] X. Ni, Z. J. Wong, M. Mrejen, Y. Wang, and X. Zhang, *Science* **349**, 1310 (2015).
- [5] N. Yu, P. Genevet, M. A. Kats, F. Aieta, J.-P. Tetienne, F. Capasso, and Z. Gaburro, *Science* **334**, 333 (2011).
- [6] S. Sun, Q. He, S. Xiao, Q. Xu, X. Li, and L. Zhou, *Nat. Mater.* **11**, 426 (2012).
- [7] X. Ni, A. V. Kildishev, and V. M. Shalaev, *Nat. Commun.* **4**, 2807 (2013).
- [8] M. W. Klein, C. Enkrich, M. Wegener, and S. Linden, *Science* **313**, 502 (2006).
- [9] G. A. Wurtz, R. Pollard, W. Hendren, G. Wiederrecht, D. Gosztola, V. Podolskiy, and A. V. Zayats, *Nat. Nanotechnol.* **6**, 107 (2011).
- [10] M. Kauranen and A. V. Zayats, *Nat. Photonics* **6**, 737 (2012).
- [11] C. M. Soukoulis and M. Wegener, *Nat. Photonics* **5**, 523 (2011).
- [12] N. Yu and F. Capasso, *Nat. Mater.* **13**, 139 (2014).
- [13] N. Meinzer, W. L. Barnes, and I. R. Hooper, *Nat. Photonics* **8**, 889 (2014).
- [14] H.-H. Hsiao, C. H. Chu, and D. P. Tsai, *Small Methods* **1**, 1600064 (2017).
- [15] G. Li, S. Zhang, and T. Zentgraf, *Nat. Rev. Mater.* **2**, 17010 (2017).
- [16] P. Genevet, F. Capasso, F. Aieta, M. Khorasaninejad, and R. Devlin, *Optica* **4**, 139 (2017).
- [17] V. G. Kravets, A. V. Kabashin, W. L. Barnes, and A. N. Grigorenko, *Chem. Rev.* **118**, 5912 (2018).
- [18] P. Nordlander, C. Oubre, E. Prodan, K. Li, and M. Stockman, *Nano Lett.* **4**, 899 (2004).
- [19] A. Dmitriev, T. Pakizeh, M. Käll, and D. S. Sutherland, *Small* **3**, 294 (2007).
- [20] A. M. Funston, C. Novo, T. J. Davis, and P. Mulvaney, *Nano Lett.* **9**, 1651 (2009).
- [21] N. J. Halas, S. Lal, W.-S. Chang, S. Link, and P. Nordlander, *Chem. Rev.* **111**, 3913 (2011).
- [22] D. Gómez, Z. Teo, M. Altissimo, T. Davis, S. Earl, and A. Roberts, *Nano Lett.* **13**, 3722 (2013).
- [23] S. J. Barrow, D. Rossouw, A. M. Funston, G. A. Botton, and P. Mulvaney, *Nano Lett.* **14**, 3799 (2014).
- [24] Y.-C. Chang, S.-M. Wang, H.-C. Chung, C.-B. Tseng, and S.-H. Chang, *ACS Nano* **6**, 3390 (2012).
- [25] M. Noginov, G. Zhu, A. Belgrave, R. Bakker, V. Shalaev, E. Narimanov, S. Stout, E. Herz, T. Suteewong, and U. Wiesner, *Nature (London)* **460**, 1110 (2009).
- [26] R. F. Oulton, V. J. Sorger, T. Zentgraf, R.-M. Ma, C. Gladden, L. Dai, G. Bartal, and X. Zhang, *Nature (London)* **461**, 629 (2009).
- [27] T. Pakizeh, M. Abrishamian, N. Granpayeh, A. Dmitriev, and M. Käll, *Opt. Express* **14**, 8240 (2006).
- [28] R. Verre, Z.-J. Yang, T. Shegai, and M. Kall, *Nano Lett.* **15**, 1952 (2015).
- [29] S. Choudhary, I. De Leon, S. Swiecicki, K. M. Awan, S. A. Schulz, J. Upham, M. Z. Alam, J. E. Sipe, and R. W. Boyd, *Phys. Rev. A* **100**, 043814 (2019).
- [30] M. B. Ross, C. A. Mirkin, and G. C. Schatz, *J. Phys. Chem. C* **120**, 816 (2016).

- [31] N. S. Mueller, B. G. Vieira, F. Schulz, P. Kusch, V. Oddone, E. B. Barros, H. Lange, and S. Reich, *ACS Photonics* **5**, 3962 (2018).
- [32] R. Kim, K. Chung, J. Y. Kim, Y. Nam, S. H. K. Park, and J. Shin, *ACS Photonics* **5**, 1188 (2018).
- [33] B. G. Vieira, N. S. Mueller, E. B. Barros, and S. Reich, *J. Phys. Chem. C* **123**, 17951 (2019).
- [34] D. Hoeing, F. Schulz, N. S. Mueller, S. Reich, and H. Lange, *J. Chem. Phys.* **152**, 064710 (2020).
- [35] K. L. Kelly, E. Coronado, L. L. Zhao, and G. C. Schatz, *J. Phys. Chem. B* **107**, 668 (2003).
- [36] C. F. Bohren and D. R. Huffman, *Absorption and Scattering of Light by Small Particles* (Wiley, Hoboken, NJ, 2008).
- [37] L. Novotny, *Phys. Rev. Lett.* **98**, 266802 (2007).
- [38] I. Zoric, M. Zach, B. Kasemo, and C. Langhammer, *ACS Nano* **5**, 2535 (2011).
- [39] J. E. Sipe and J. V. Kranendonk, *Can. J. Phys.* **53**, 2095 (1975).
- [40] Y. D. Chong, L. Ge, H. Cao, and A. D. Stone, *Phys. Rev. Lett.* **105**, 053901 (2010).
- [41] A. Krasnok and A. Alú, [arXiv:1904.11384](https://arxiv.org/abs/1904.11384).
- [42] S. D. Swiecicki and J. Sipe, *J. Opt.* **19**, 095006 (2017).
- [43] P. B. Johnson and R.-W. Christy, *Phys. Rev. B* **6**, 4370 (1972).
- [44] Schott optical glass data sheets, https://refractiveindex.info/download/data/2017/schott_2017-01-20.pdf.
- [45] A. Christ, O. J. Martin, Y. Ekinici, N. A. Gippius, and S. G. Tikhodeev, *Nano Lett.* **8**, 2171 (2008).
- [46] A. Alabastri, X. Yang, A. Manjavacas, H. O. Everitt, and P. Nordlander, *ACS Nano* **10**, 4835 (2016).
- [47] M. Urbietta, M. Barbry, Y. Zhang, P. Koval, D. Sánchez-Portal, N. Zabala, and J. Aizpurua, *ACS Nano* **12**, 585 (2018).
- [48] J. Zhang, K. F. MacDonald, and N. I. Zheludev, *Light: Sci. Appl.* **1**, e18 (2012).
- [49] W. Tan, C. Zhang, C. Li, X. Zhou, X. Jia, Z. Feng, J. Su, and B. Jin, *Appl. Phys. Lett.* **110**, 181111 (2017).
- [50] R. Alaei, M. Albooyeh, and C. Rockstuhl, *J. Phys. D* **50**, 503002 (2017).
- [51] W. Wan, Y. Chong, L. Ge, H. Noh, A. D. Stone, and H. Cao, *Science* **331**, 889 (2011).
- [52] D. G. Baranov, A. Krasnok, T. Shegai, A. Alú, and Y. Chong, *Nat. Rev. Mater.* **2**, 17064 (2017).
- [53] M. Z. Alam, S. A. Schulz, J. Upham, I. De Leon, and R. W. Boyd, *Nat. Photonics* **12**, 79 (2018).
- [54] J. J. Saarinen and J. Sipe, *J. Mod. Opt.* **55**, 13 (2008).